

Pre-collapse spaceborne deformation monitoring of the Kakhovka dam, Ukraine, from 2017 to 2023

Tavakkoliestahbanati, Amin; Milillo, Pietro; Kuai, Hao; Giardina, Giorgia

DOI

[10.1038/s43247-024-01284-z](https://doi.org/10.1038/s43247-024-01284-z)

Publication date

2024

Document Version

Final published version

Published in

Communications Earth and Environment

Citation (APA)

Tavakkoliestahbanati, A., Milillo, P., Kuai, H., & Giardina, G. (2024). Pre-collapse spaceborne deformation monitoring of the Kakhovka dam, Ukraine, from 2017 to 2023. *Communications Earth and Environment*, 5(1), Article 145. <https://doi.org/10.1038/s43247-024-01284-z>

Important note

To cite this publication, please use the final published version (if applicable). Please check the document version above.

Copyright

Other than for strictly personal use, it is not permitted to download, forward or distribute the text or part of it, without the consent of the author(s) and/or copyright holder(s), unless the work is under an open content license such as Creative Commons.

Takedown policy

Please contact us and provide details if you believe this document breaches copyrights. We will remove access to the work immediately and investigate your claim.

<https://doi.org/10.1038/s43247-024-01284-z>

Pre-collapse spaceborne deformation monitoring of the Kakhovka dam, Ukraine, from 2017 to 2023

Check for updates

Amin Tavakkoliestahbanati¹ ✉, Pietro Milillo^{1,2}, Hao Kuai³ & Giorgia Giardina³

The Kakhovka Dam on the Dnieper River in Kherson Oblast, Ukraine, was completed in 1956 as the final dam in the Dnieper reservoir cascade. On the morning of June 6th, 2023, a substantial portion of the dam suffered a collapse while under Russian control. This incident was documented through satellite optical and radar images, providing valuable evidence of the dam's condition. Here we present the results of multi-temporal Interferometric Synthetic Aperture Radar (MT-InSAR) monitoring of the Kakhovka dam. The dam is vital for water management and hydroelectric power generation. Utilizing multi-temporal InSAR (MT-InSAR) data, we assessed the dam deformations prior to the collapse. Our findings indicate movements of the south side, facing the Dniprovska Gulf, compatible with several possible damage mechanisms. This study highlights the significance of employing spaceborne advanced monitoring techniques to detect signs of distress and ensure the stability of critical infrastructure.

The Kakhovka Dam, situated on the Dnieper River in Kherson Oblast, Ukraine, was completed in 1956 as the final dam in the Dnieper reservoir cascade. Its main objectives encompass hydroelectric power generation, irrigation, and navigation.

The Kakhovka Reservoir has a storage capacity of 18 cubic kilometers and provides water for cooling the 5.7 GW Zaporizhzhia Nuclear Power Plant and irrigation in southern Ukraine and northern Crimea¹. The dam's central section comprised an overflow dam, a hydroelectric power station, and a navigation lock (green marker in Fig. 1). Two earth dams are connected to this central section, as illustrated by the blue polygons in Fig. 1. A road and a railway crossed the Dnieper River on the dam. During the Russian invasion of Ukraine, notable developments pertaining to the Kakhovka dam in southern Ukraine came to light through the analysis of Maxar satellite images acquired on November 11th, 2022. These images revealed notable new damage to the dam after Russia's withdrawal from the adjacent city of Kherson². On June 2nd, 2023, satellite images released by Planet Lab, a private Earth imaging company specialized in daily high-resolution monitoring, identified road damage to the bridge³.

Furthermore, on the morning of June 6th, 2023, a substantial portion of the Nova Kakhovka dam suffered a collapse while under Russian control. This incident was documented through satellite optical images released by Planet Lab, providing valuable evidence of the dam's condition³. The dam segment is a concrete gravity dam measuring 29 meters in height and 447

meters in length¹. Using a post-collapse image acquired by Umbra, a high-resolution X-band SAR, as well as pre- and post-collapse Sentinel-1 images, we identified two main breaches that had occurred at the dam (Fig. 1, Polygons II and IV). While polygon I has been affected by the events imaged before the damage, occurred on November 11th, 2022⁴, polygon III contains the breached part of the hydroelectric power plant and polygon V shows the location of an associated building (Fig. 1).

The cause of the collapse has been a subject of intense debate. Based on a Reuters report, which details an investigation conducted collaboratively by Ukrainian prosecutors and an international legal experts' team, explosive placed by Russia were identified as the cause of the collapse⁵. The New York Times reported that an American infrared intelligence satellite had recorded a heat signal over the dam before the collapse⁶. Moreover, seismic signals, likely from a large explosion, were recorded by sensors located in Ukraine and Romania by NORSAR^{6,7}. Based on these findings, The New York Times suggested that the explosion at the dam was caused by Russian invasion forces⁵. Chances of structural failure have been assessed as low, providing the dam was maintained properly⁸. Additional theories included the possible influence of earlier damage and of increased water levels⁹. The Conflict Intelligence Team observed that the dam was operating abnormally, with only the same spillway gates open, for eight months starting from November 15th, 2022¹⁰. During this period, gates were open only on the east side¹⁰ (Fig. 1, polygon II).

¹Department of Civil and Environmental Engineering, University of Houston, Houston, TX, USA. ²German Aerospace Center (DLR), Microwaves and Radar Institute, Munich, Germany. ³Department of Geoscience and Engineering, TU Delft, Delft, Netherlands. ✉ e-mail: atavakk3@cougarnet.uh.edu

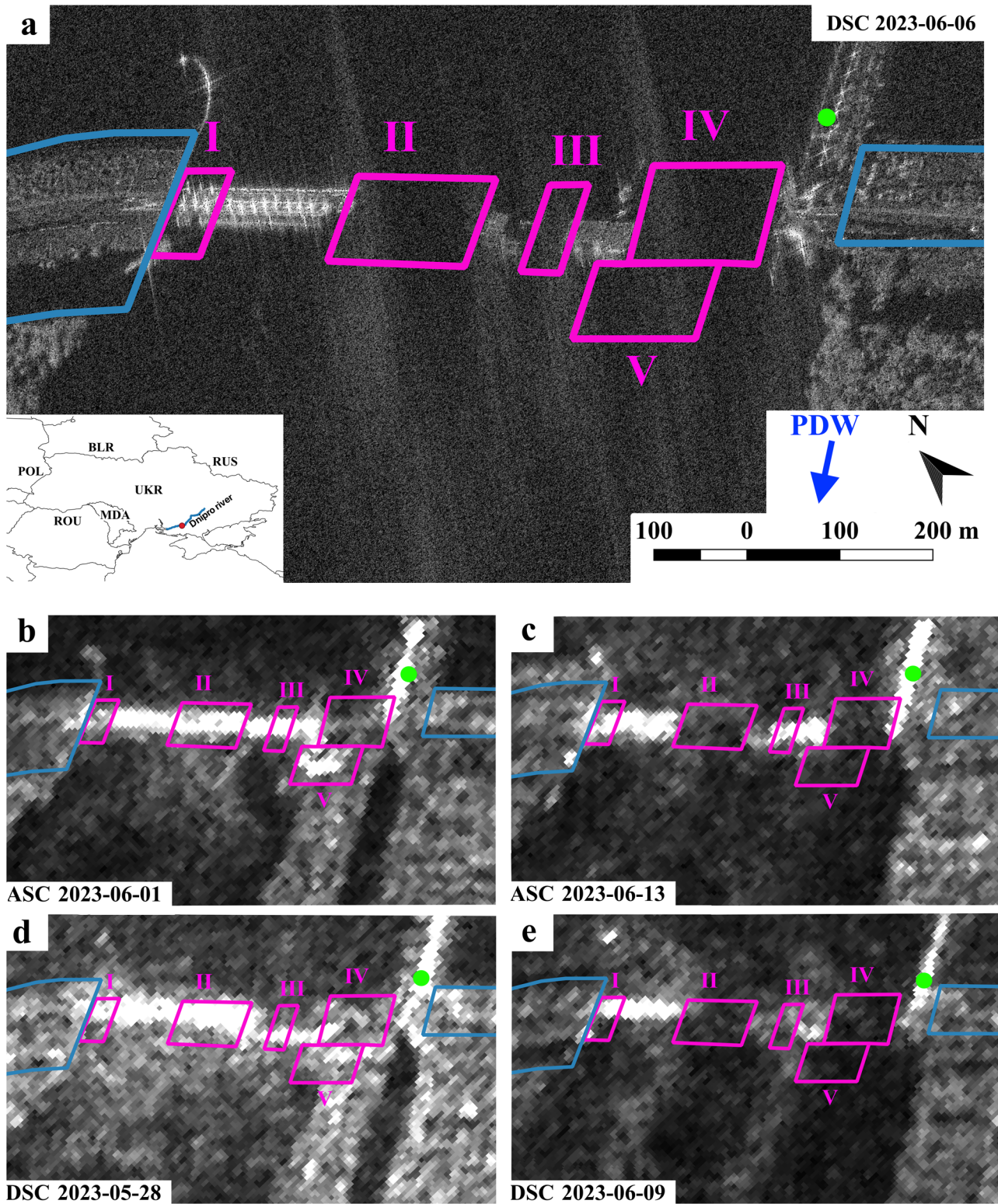


Fig. 1 | Areas of interest over the Kakhovka dam identified using Umbra HH polarized and Sentinel-1 VV polarized GRD images. **a** shows the Umbra descending image with the resolution of 50 by 50 cm, acquired on June 6th 2023. **b** and **c** show two Sentinel-1 SAR amplitude using ascending images acquired on June 1st 2023 and June 13th 2023 before and after the collapse, respectively. Similarly, **d** and **e** show the Sentinel-1 SAR amplitude using descending images acquired on May

28th 2023 and June 9th 2023, respectively. The purple numbered polygons represent the collapsed parts of the dam. The blue polygons indicate the dam embankments. The green marker indicates the shipping lock location. The blue arrow shows the direction of the river flows. SAR data © 2023 Umbra Lab, Inc. (Licensed under CC BY 4.0). Copernicus Sentinel data 2023, processed by ESA.

In a war scenario context, the application of remote sensing methodologies becomes pivotal for obtaining vital information regarding critical infrastructure^{11–14}. Multi-temporal Interferometric Synthetic Aperture Radar (MT-InSAR) is a technique that exploits a stack of interferometric SAR data, to extract measurements of ground surface displacement through the analysis of radar phase echoes. In the past 20 years MT-InSAR has proven to be an effective methodology to measure structural displacement characterizing a diverse set of infrastructure including bridges^{15,16}, levees and dams^{11,17–21}. Here we present an extensive multi-geometry cumulative deformation map of the Kakhovka dam in Southern Ukraine, using measurements derived from space-borne MT-InSAR²¹. Through our analysis, we observed displacements characterizing different segments of dam, up to two years prior to the actual collapse. Notably, no deformation was detected during the period spanning from 2015 to May 2023 for polygons I–III. However, vertical deformation started in June 2021 for polygon II and IV, while, in June 2022, coinciding with the increase in Kakhovka reservoir water level²², horizontal deformation over certain parts of the dam (polygon II and IV) began to manifest, indicating signs of distress characterizing the dam. By leveraging the high temporal resolution of the Sentinel-1 Synthetic Aperture Radar (SAR) data, we have been able to quantify the extent and timing of deformation at the Kakhovka dam.

Results

We used two Sentinel-1 InSAR dataset comprising both ascending and descending tracks. The ascending (ASC) track included a total of 180 images acquired by Sentinel-1A and Sentinel-1B, spanning from July 2017 to June 2023 (Table 1). Similarly, the descending (DSC) track dataset consisted of 226 images acquired by Sentinel-1A and Sentinel-1B, covering the period from November 2015 to June 2023. By analyzing the time-series of deformation over each of the five polygons (Fig. 1), five distinct patterns of deformation were observed in both the ASC and DSC geometries, indicating the presence of displacement in different directions, including vertical (up/down) and horizontal (east/west) (Fig. 2 and Table 2). It is noteworthy that upon analysing the data, it becomes apparent that polygons I and III remained remarkably stable, with no substantial deformation observed throughout the entire period. In contrast, polygons II, IV, and 5 exhibited the most pronounced changes, particularly starting from June 2021. Polygon V, which is situated above a nearby dam facility, shows a linear deformation trend starting in 2015. This trend reached a rate of nearly 2±0.2 mm per year, amounting to a cumulative displacement of 10 mm over the 5 years prior to the collapse (Fig. 2h). Starting in June 2021, the rate of deformation in polygon V accelerated by 4 times, reaching a trend of 8.3±0.7 mm year⁻¹ until the dam’s collapse (Fig. 2h). Conversely, polygons II and IV, which are positioned over the section of the dam that experienced breaches, exhibit an average deformation of 21.5±1.5 mm year⁻¹ and 12±1.8 mm year⁻¹ for the ascending and descending geometries, respectively (Fig. 2b, c, f, g). Figure 3 illustrates the distribution of selected persistent scatters (PSs) along with their respective mean velocities, including both ASC and DSC geometries. The ascending track perspective is observed from the southern side of the dam (see Fig. 2a, c), characterized by a smaller look angle compared to the descending (Table 1). Consequently, the chosen PSs are primarily located in the southern portion of the dam. Conversely, the descending track is characterized by a higher look angle, and it originates from the northern side, resulting in PSs that encompass both the northern and southern regions of the dam. Therefore, for a fair comparison, the observed deformation in these polygons is localized and confined to the southern side of the dam. The DSC dataset reveals slightly lower velocity

values and similar activation dates due to its reduced sensitivity to vertical displacements as the descending is characterized by a larger look angle, (Tables 1 and 2).

Ascending and descending geometries present dissimilar patterns, suggesting the presence of vertical (up/down) and horizontal (east/west) displacements. To gain a more comprehensive understanding, the average line-of-sight (LOS) deformation values were further analysed and decomposed into their vertical and perpendicular to the dam walls (PDW) components (Table 3). Specifically, over polygon II we measured a downward linear displacement of -22.7 ± 0.3 mm year⁻¹ starting from June 2021 and a 28.3 ± 0.3 mm year⁻¹ upstream PDW displacement starting from June 2022. In contrast, polygon IV exhibits a downward displacement of approximately -20.3 ± 0.3 mm year⁻¹ initiating in June 2021, and a 21.3 ± 0.2 mm year⁻¹ upstream PDW displacement, initiating in June 2022 (Table 3 and Fig. 4). Time-series of decomposed deformations along the vertical and PDW components for polygon II, polygon IV and polygon V are represented in Fig. 4. The time-series of measured water levels using the Hydroweb River Water Level products²² is also plotted as the second axis for each panel in Fig. 4.

Discussion

Based on previous studies over four hydroelectric dams in Ukraine²³, from February to August points located on the surface of all dam walls move horizontally toward the reservoir and rise vertically. From August to February, on the contrary, all points move in the opposite direction²³. This pattern is a manifestation of thermal dilation²⁴. Therefore, to highlight potential anomalous trends uncorrelated with thermal displacements it is necessary to remove the thermal dilation term from the InSAR deformation signal. To this end, we fit a linear model to InSAR deformation and to weather temperature data acquired from the Visual Crossing service²⁵ at the acquisition date.

The thermally detrended vertical and PDW displacements indicate that between 2017 and June 2021 an area located next to the Kakhovka hydroelectric power plant has been almost steady (Polygon III). This area was subsiding in the past²⁶ since compression of the clay layers underlying the infrastructure has been recorded between 1955 and 1976 at rates of 60 mm year⁻¹. A nearby facility has been subsiding from 2017 to June 2021 by an average constant rate of -2.4 ± 0.2 mm year⁻¹ (polygon V). Using the method in Raspini et al.²⁷ we identified an accelerating subsidence pattern starting June 2021. In June 2021, the facility started settling at 8.8 mm year⁻¹ rates, four times faster compared to the subsidence rate before acceleration. In June 2021, the concrete dam started showing signs of accelerating subsidence movements at maximum rates of -22.7 ± 0.3 mm year⁻¹ and -20.3 ± 0.3 mm year⁻¹, respectively, over polygons II and IV (Fig. 4). In addition to the vertical deformation, Figs. 4b and d exhibit upstream PDW movements in both polygon II and polygon IV. A comparison of Fig. 4e and f indicates that the most dominant component of deformation for polygon V was vertical.

We then analyzed the correlation between water levels and the PDW component of the MT-InSAR cumulative displacements. First, we computed the correlation coefficient between water level fluctuations and PDW deformation component from mid-2017 to the end of 2021, considering a zero-day time lag, for the PSs located over the southern side of the dam. Even though we do not observe long-term upstream motion of the PDW component between 2017–2023, as shown in Fig. 4b, d, the results uncover a negative correlation of -0.57 and -0.62 between water level changes and the corresponding deformation time series for polygon II and polygon IV,

Table 1 | Sentinel-1 InSAR Processing: Acquisition information for ascending and descending tracks

Flight direction	IW	Orbit number	Look angle (deg)	Heading angle (deg)	Number of images	First date	Last date	Versors		
								North	East	Up
Descending	1	65	43.66	-10.82	226	November 2015	May 2023	-0.12	0.67	-0.72
Ascending	3	14	33.79	-170.82	180	July 2017	May 2023	-0.08	-0.54	-0.83

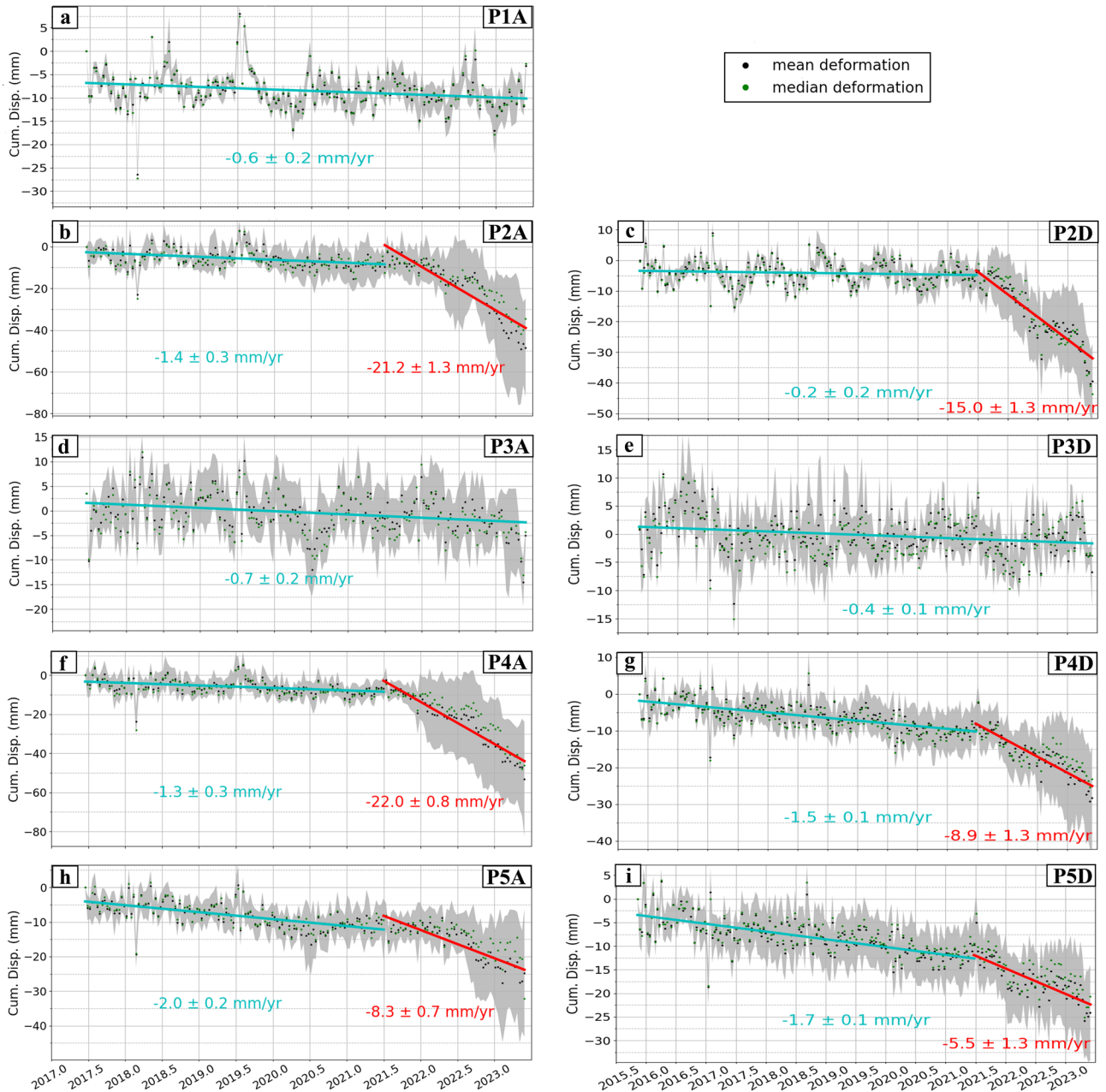


Fig. 2 | Average line of sight deformation time-series for polygons I, II, III, IV, and V extracted from Fig. 1. Images a, d, f and h represent the ascending deformation time-series and images c, e, g and i are the descending deformation time-series, respectively. Positive values point to moving toward the satellite. The Cyan line represents trends between the beginning of each time-series and June 2021 while the red lines indicate trends observed during the period July 2021–2023. Mean and median deformation is represented as black and green dots respectively. Grey

error bars represent limits indicating one standard deviation. The titles of the panels have been abbreviated for clarity, following the pattern: Px(A/D), where “P” represents “Polygon”, x is the number indicating the polygon number, and “A” or “D” stands for “ascending” or “descending” geometry, respectively. Just one measurement point has been found for polygon I descending (PID) and therefore has not been displayed in this figure.

Table 2 | Sentinel-1 InSAR deformation rates for both ascending and descending track over polygons I-IV

Flight direction	Polygon I (mm yr ⁻¹)	Polygon II (mm yr ⁻¹)	Polygon III (mm yr ⁻¹)	Polygon IV (mm yr ⁻¹)	Polygon V (mm yr ⁻¹)
Ascending	-0.6±0.2	-21.2±1.3	-0.7±0.2	-22±0.8	-8.3±0.7
Descending	-	-15±1.3	-0.4±0.1	-8.9±1.3	-5.5±1.3

For polygons II, IV, and V rates are calculated since June 23, 2021 to May 28, 2023 and for polygons I and III rates are calculated since the first acquisition date of each track to May 28, 2023. Positive values point to moving toward the satellite.

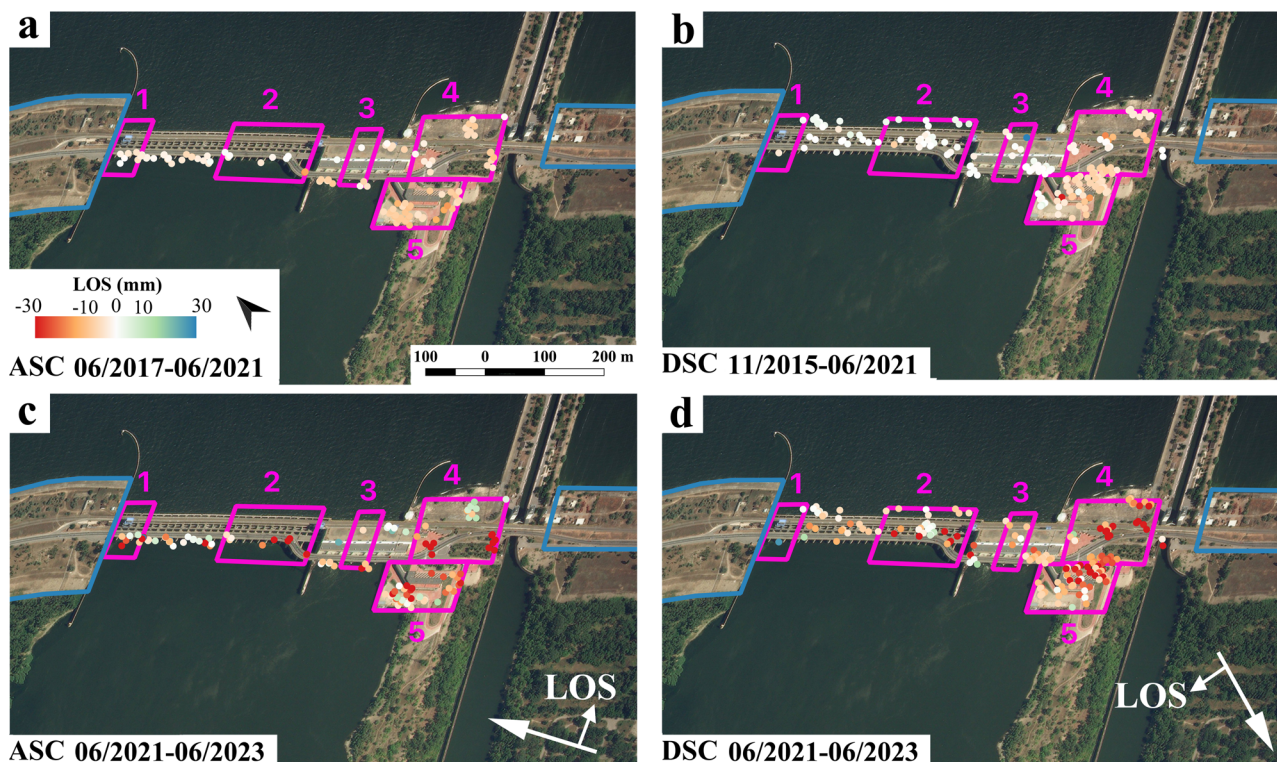


Fig. 3 | Mean velocity maps showing the location of the measurement points. a and b show pre-event velocity maps for ascending and descending tracks, respectively. c and d represent velocity maps after deformation acceleration begin for

both ascending and descending geometries, respectively. Negative values point to moving away from the satellite. Map data: Bing, © 2023 TomTom, © 2023 Maxar (<https://www.bing.com/maps>).

Table 3 | Decomposed deformation time-series over polygons I-V since June 1, 2021 to May 28, 2023

Deformation component	Polygon I (mm yr ⁻¹)	Polygon II (mm yr ⁻¹)	Polygon III (mm yr ⁻¹)	Polygon IV (mm yr ⁻¹)	Polygon V (mm yr ⁻¹)
Vertical	–	–22.7±0.3	–1.2±0.1	–20.3 ± 0.3	–8.8±0.1
PDW	–	28.3±0.3	0.0±0.2	21.3±0.2	5.3±0.1

Positive values indicate upward deformation for the vertical component and upstream deformation for the PDW component.

respectively (Supplementary Fig. 1a and Supplementary Fig. 1b). The correlation coefficients over polygon II and IV for zero-day time-lag remained approximately the same between June 09th, 2022 and June 1st, 2023, 5 days before the collapse (Supplementary Fig. 1c and Supplementary Fig. 1d). This indicates a linear relationship between decreasing water level in the dam basin and movement along the PDW component of the dam. To confirm this conclusion, we also analysed the correlation between water levels and the PDW component of the MT-InSAR cumulative displacements on other parts of the dam. Our data reveal a similar negative correlation between points situated amidst polygon I and polygon II (Supplementary Fig. 2a), as well as those positioned between polygon III and polygon IV (Supplementary Fig. 2b). Nevertheless, it is worth noting that the PDW displacement component of the road segment spanning from polygon II to polygon III does not exhibit any significant correlation with changes in water level, probably due to the amount and the spatial distribution of the measurement points (Supplementary Fig. 2c). With the rise in water level changes from 2022 onward, the PDW component of the deformation signal becomes more pronounced over polygons II and IV, maintaining their correlation with basin water levels, and reaching rates of about 28.3 ± 0.3 mm year⁻¹ upstream. Such increased rate does not affect the portions of the dam where signs of structural distress did not manifest (i.e. between polygon I and II, III and IV Fig. 3).

Overall, the observed vertical and horizontal displacements are compatible with different possible damage mechanisms. In addition to

overtopping, the deformations monitored suggest compatibility with a possible lack of maintenance during the Russian invasion. This includes issues such as faulty gate operation and the accumulation of sediment and debris. All these mechanisms can lead to damage at the level of the dam foundations^{28–30}.

Despite some well recognized limitations and challenges³¹, InSAR’s ability to detect and quantify ground movements with high precision and over extended periods of time contributes to enhanced risk assessment, forensic engineering activities and informed decision-making processes. Current hypotheses ascribe the collapse of the dam to an explosion occurred on June 6th, 2023. Although InSAR data cannot exclude an explosion occurred on that date, they can identify existing damage mechanisms that might have affected the dam prior to its collapse. Our data support the hypothesis that the structure was moving downward since June 2021 way before the beginning of the war. With the beginning of the war, neglected dam maintenance and operations might have destabilized the structure over specific areas, favouring the development of the above-mentioned mechanisms. The findings of this research provide valuable insights for dam management and highlight the potential of InSAR as a proactive monitoring tool for infrastructure stability assessment.

Conclusions

In this paper, we showed the results of a multi-temporal SAR interferometric techniques to extract deformation over the Kakhovka dam.

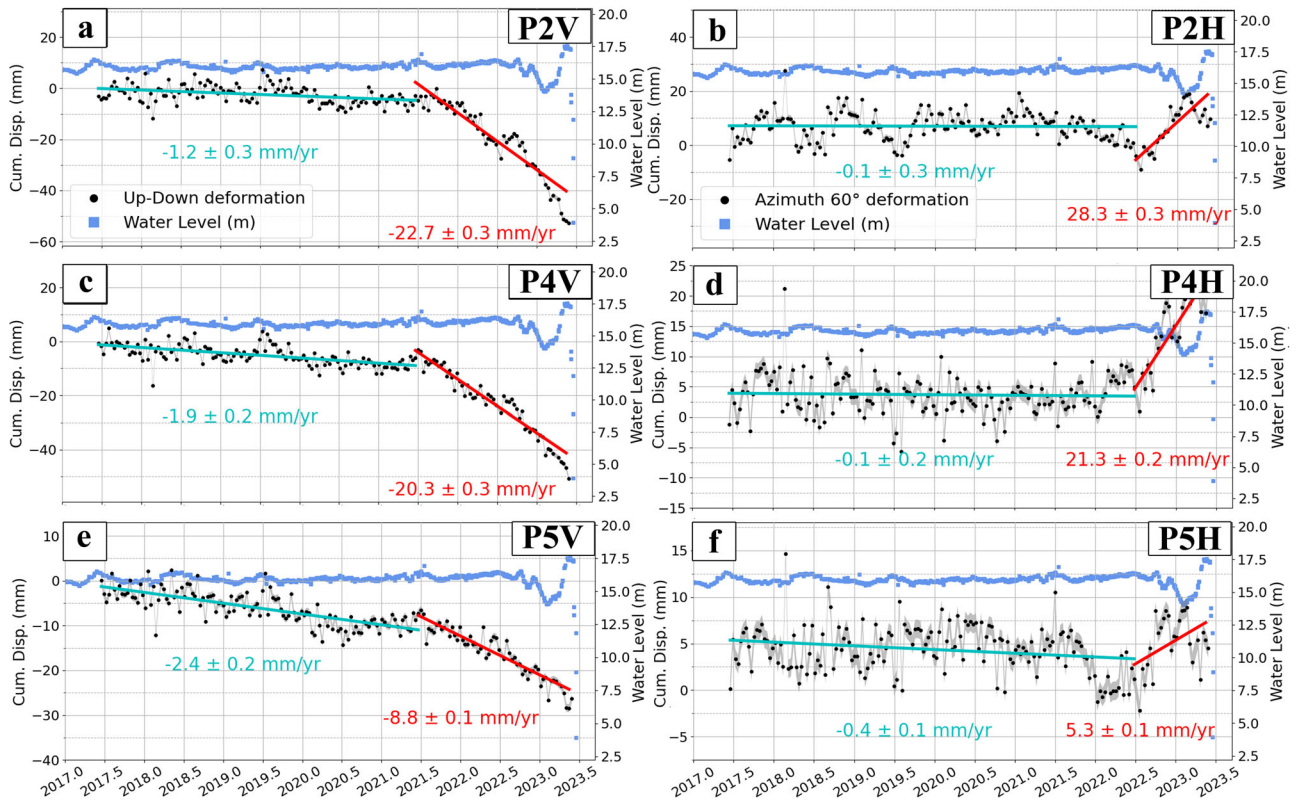


Fig. 4 | Decomposed deformation time-series for polygons II, IV and V. a and b represent the vertical and PDW deformation components for polygon II, respectively. c and d show the vertical and PDW averaged deformation time series for polygon IV, respectively. e and f show the vertical and PDW averaged deformation time series for polygon V, respectively. Positive values indicate upward motion for the vertical component and along upstream motion for the PDW

component. The titles of the panels have been abbreviated for clarity, following the pattern: Px(V/H), where “P” represents “Polygon”, x is the number indicating the polygon number, and “V” or “H” stands for “vertical” or “horizontal” (PDW) component, respectively. Blue squares show the water level of the reservoir time-series from Hydroweb²².

The interferometric analysis captured both spatial and temporal patterns of movement, enabling the identification and characterization of deformation hotspots prior to the dam collapse. The detected displacements included mainly subsidence initiated in June 2021 and eastward lateral movements initiated in June 2022. The PDW movements show a linear correlation with changes in water levels. The observed mechanisms are compatible with the effect of possible overtopping, sediment and debris build-up, or faulty gate operation. This study demonstrates the effectiveness of InSAR as a remote sensing technique for monitoring critical and strategic structures such as dams.

Methods

The process of retrieving deformation values can be divided into two main steps. First, SARPROZ was utilized to perform MT-InSAR³¹, enabling the filtering of the thermal dilation component and the extraction of deformation information from the SAR data. Finally, deformation vector decomposition was applied to analyze the three-dimensional components of the dam’s deformation.

Multi-temporal InSAR Analysis

Differential InSAR (DInSAR) is a technique used to measure deformation between two image acquisitions. In DInSAR, interferometric phases are calculated by multiplying the complex conjugate of two complex coregistered single look complex (SLC) data. Multi-temporal InSAR (MT-InSAR), on the contrary, leverages multiple repeat-pass interferometric pairs to create a time-series of deformation. To obtain a time-series, it is necessary for each pair of images to share either the same primary or secondary acquisition date. Interferometric phases consist of

several components including, topography, deformation, and atmospheric phase screen (APS)³²:

$$\Delta\theta_{\text{ifg}} = \Delta\theta_{\text{flat}} + \Delta\theta_{\text{topo}} + \Delta\theta_{\text{defo}} + \Delta\theta_{\text{atm}} \quad (1)$$

Where the flat earth, $\Delta\theta_{\text{flat}}$, and topography, $\Delta\theta_{\text{topo}}$, components can be reduced using orbital information and a pre-existing Digital Elevation Model (DEM). Here a Shuttle Radar Topography Mission (SRTM) DEM with 30-meter resolution is used to compensate for the topographic component. Moreover, given that the analysis is focused on a relatively small area, the APS, $\Delta\theta_{\text{atm}}$, phase component can be considered to be correlated and consistent across the entire area, and therefore can be ignored. After removing those components, the interferometric phases, $\Delta\theta_{\text{ifg}}$, becomes the summation of the residual topography and deformation signal. Here we used the SARPROZ software^{33,34} to infer the time-series of surface deformation.

The process of linking interferograms is known as graph connection, and there are various approaches to accomplish it. One of these approaches is the star graph method, where one of the single look complex (SLC) images is chosen as the primary, while the remaining images are considered as secondary images. As a result, for N images, there will be N-1 interferograms. We adopted the persistent scatterer Interferometry approach³⁵ focusing only on points that exhibit stable electromagnetic behavior throughout the entire acquisition period. To select our potential measurement points, here we used the amplitude stability index (ASI) criterion

defined in Eq. 2:

$$ASI_i = 1 - \frac{\sigma_i}{\mu_i} \quad (2)$$

where i is the pixel number, σ is the standard deviation of each scatterers' amplitude across time and μ is the scatterers' mean value across time. The ASI has a maximum value of 1, indicating that a pixel has maintained a consistent amplitude value over time. Therefore, a higher ASI can be considered as a proxy for more stable scatterer. In this study, a threshold of 0.7 was used for PS selection.

The subsequent step involved retrieving unwrapped phases from the wrapped phases, considering that they are in the complex domain. In other words, unwrapping is the process of retrieving the exact number of integer cycles, as interferometric phases are modulated between 0 and 2π ³⁶. As mentioned earlier, the two components to be estimated are deformation and residual height. To address this, the temporal coherence $\gamma_{temporal}$, obtained by averaging the interferometric phases of the PSs and subtracting the topography and deformation model, can serve as a model to be optimized:

$$\gamma_{temporal} = \frac{1}{N} \sum_{i=1}^N e^{j\Delta\varphi} \times e^{-jM_{(h,defo)}} \quad (3)$$

where N is the number of images, $\Delta\varphi$ is the wrap interferometric phases and $M_{(h,defo)}$ is a model defined based the deformation and residual height. To solve this model, SARPROZ employs the periodogram method, where the optimal values for the unknowns are obtained by maximizing the periodogram³⁷. In this study, a five-degree polynomial was utilized as the deformation model³³.

A posteriori, after inferring time-series of surface displacement for each measurement point we focused on the hydrologically correlated deformation signals while filtering out the thermal component of displacement¹⁶. By analyzing scatter plots, indicating the time-series of deformation versus temperature, we can identify a linear relation between these two variables. Equation 4 represents the model that defines the relation between InSAR deformation and weather temperature:

$$T = a \times d_{los} + b \quad (4)$$

where T represents the weather temperature in Celsius, d_{los} represents the deformation along the line of sight in millimeters, and a and b are the unknown coefficients. Temperature data were obtained from the Visual Crossing website²⁵. Before fitting a model to retrieve two unknowns, an outlier detection was performed on the dataset. Once the outliers were removed, the model was fitted, and the thermal component of the deformation signal was calculated. Subsequently, if the correlation coefficient between deformation and weather temperature exceeded 0.7, the estimated thermal component was subtracted from the LOS deformation signal. A similar approach was used to assess correlation with hydrologically correlated deformation using Hydroweb River Water Level products.

Pseudo-3D decomposition

InSAR measures the deformation only along the LOS. This means that it is not possible to determine whether a scatterer is moving down or up solely based on the InSAR data acquired with one geometry. Furthermore, InSAR is almost insensitive to deformations along the flight direction which in the case of Sentinel-1 corresponds to almost the north-south direction (Table 1). In Eq. 4, both the ascending track and descending track data are used to perform the inversion and retrieve the up-down and east-west deformation

components.

$$d_{los} = \sin \theta * \cos \beta * d_{east-west} - \cos \theta * d_{up-down}$$

$$\begin{bmatrix} d_{los_{descending}} \\ d_{los_{ascending}} \end{bmatrix} = \begin{bmatrix} \cos \beta_{asc} * \sin \theta_{asc} - \cos \theta_{asc} \\ \cos \beta_{desc} * \sin \theta_{desc} - \cos \theta_{desc} \end{bmatrix} * \begin{bmatrix} d_{east-west} \\ d_{up-down} \end{bmatrix} \quad (5)$$

where β and θ are the headings and look angle of each track, respectively (Table 1). To align these two datasets, a stable reference point with the following latitude: 46.7668 and longitude: 33.3721, was used. The same stable reference point was used for processing both ascending and descending data in SARPROZ.

Data availability

Sentinel-1 images are readily accessible for download from the Copernicus Open Access Hub. SAR data © 2023 Umbra Lab, Inc. (Licensed under CC BY 4.0). Water level data can be obtained from the Hydroweb River Water Level product. Weather temperature information for each acquisition date can be sourced from the Visual Crossing website. All data needed to evaluate the conclusions in the paper are present in the paper and/or the Supplementary Materials and on Dryad repository [https://doi.org/10.5281/zenodo.10452427].

Code availability

Sentinel-1 images are processed using SARPROZ software (https://www.sarproz.com/application-form/). Deformation maps are generated by QGIS (https://qgis.org/en/site/).

Received: 28 September 2023; Accepted: 22 February 2024;
Published online: 03 April 2024

References

1. Vyshnevskiy, V., Shevchuk, S., Komorin, V., Oleynik, Y. & Gleick, P. The destruction of the Kakhovka dam and its consequences. *Water Int.* **48**, 631–647 (2023).
2. Maxar publishes updated satellite imagery of Kakhovka dam destruction. (n.d.). Retrieved July 24, 2023, from https://kyivindependent.com/new-satellite-images-show-flooding-from-kakhovka-dam-destruction/.
3. Satellite Imagery Gallery | Planet. (n.d.). Retrieved December 24, 2023, from https://www.planet.com/gallery/#!/post/destruction-of-the-kakhovka-dam.
4. New damage to major dam near Kherson after Russian retreat -Maxar satellite | Reuters. (n.d.). Retrieved 10 November 2023, from https://www.reuters.com/world/europe/new-damage-major-dam-near-kherson-after-russian-retreat-maxar-satellite-2022-11-11/.
5. Ukraine says Kakhovka dam collapse caused 1.2 billion euros in damage | Reuters. (n.d.). Retrieved 8 November 2023, from https://www.reuters.com/world/europe/ukraine-says-kakhovka-dam-collapse-caused-12-billion-euros-damage-2023-06-20/.
6. Why the Evidence Suggests Russia Blew Up the Kakhovka Dam - The New York Times. (n.d.). Retrieved 8 November 2023, from https://www.nytimes.com/interactive/2023/06/16/world/europe/ukraine-kakhovka-dam-collapse.html.
7. Seismic signals recorded from an explosion at the Kakhovka Dam in Ukraine June 6th, 2023 - NORSAR. (n.d.). Retrieved December 24, 2023, from https://www.norsar.no/in-focus/seismic-signals-recorded-from-an-explosion-at-the-kakhovka-dam-in-ukraine.
8. Nova Kakhovka dam: Here are the key theories on what caused Ukraine's catastrophic dam collapse | CNN. (n.d.). Retrieved 8 November 2023, from https://www.cnn.com/2023/06/08/europe/nova-kakhovka-destruction-theories-intl/index.html.

9. Ukraine dam: *What we know about Nova Kakhovka incident* (2023) *BBC News*. Retrieved on 13 November 2023, from <https://www.bbc.com/news/world-europe-65818705>.
10. Sitrep for Jun. 6-7, 2023 (as of 08:30 a.m.) — *Teletype*. (n.d.). Retrieved November 9, 2023, from <https://archive.ph/2023.06.19-005640/> <https://notes.citeam.org/dispatch-jun-6-7#selection-409.0-409.5>.
11. Milillo, P. et al. Space geodetic monitoring of engineered structures: The ongoing destabilization of the Mosul dam, Iraq. *Sci. Rep.* **6**, 1–7 (2016).
12. Milillo, P. et al. (2016, October). Structural health monitoring of engineered structures using a space-borne synthetic aperture radar multi-temporal approach: from cultural heritage sites to war zones. In *SAR Image Analysis, Modeling, and Techniques XVI* (10003, pp. 118–129).
13. Bolorani, A. D., Darvishi, M., Weng, Q. & Liu, X. Post-war urban damage mapping using InSAR: the case of Mosul City in Iraq. *ISPRS Int. J. Geo-Inf.* **10**, 140 (2021).
14. Aimaiti, Y., Sanon, C., Koch, M., Baise, L. G. & Moaveni, B. War related building damage assessment in Kyiv, Ukraine, using Sentinel-1 Radar and Sentinel-2 optical images. *Remote Sensing* **14**, 6239 (2022).
15. Milillo, P., Giardina, G., Perissin, D., Milillo, G., Coletta, A. & Terranova, C. Pre-collapse space geodetic observations of critical infrastructure: The Morandi Bridge, Genoa, Italy. *Remote Sensing* **11**, 1403, <https://doi.org/10.3390/RS11121403> (2019).
16. Selvakumaran, S., Sadeghi, Z., Collings, M., Rossi, C., Wright, T. & Hooper, A. Comparison of in situ and interferometric synthetic aperture radar monitoring to assess bridge thermal expansion. *Proc. Inst. Civil Eng.: Smart Infrastruct. Constr.* **175**, 73–91 (2022).
17. Wang, T., Perissin, D., Rocca, F. & Liao, M. S. Three Gorges Dam stability monitoring with time-series InSAR image analysis. *Sci. China Earth Sci.* **54**, 720–732 (2011).
18. Grebby, S. et al. Advanced analysis of satellite data reveals ground deformation precursors to the Brumadinho Tailings Dam collapse. *Commun. Earth Environ.* **2**, 2 (2021).
19. Gama, F. et al. Deformations prior to the Brumadinho dam collapse revealed by Sentinel-1 InSAR data using SBAS and PSI techniques. *Remote Sensing* **12**, 3664 (2020).
20. Wang, Q. Q., Huang, Q. H., He, N., He, B., Wang, Z. C. & Wang, Y. A. Displacement monitoring of upper Atbara dam based on time series InSAR. *Survey Review* **52**, 485–496 (2020).
21. Milillo, P. et al. Monitoring dam structural health from space: Insights from novel InSAR techniques and multi-parametric modelling applied to the Pertusillo dam Basilicata, Italy. *Int. J. Appl. Earth Obs. Geoinf.* **52**, 221–229 (2016).
22. *Hydroweb* 2023. Retrieved July 18, 2023, from https://hydroweb.theia-land.fr/collections/hydroweb/L_kakhovka?lang=en&.
23. Tretyak, K., Bisovetskiy, Y., Savchyn, I., Korlyatovych, T., Chernobyl, O., & Kukhtarov, S. Monitoring of spatial displacements and deformation of hydraulic structures of hydroelectric power plants of the Dnipro and Dnister cascades (Ukraine). *J. Appl. Geodesy* **16**, 351–360 (2023).
24. Tretyak, K. & Palianytsia, B. Dam spatial temperature deformations model development based on GNSS Data. *J. Perform. Constr. Facil.* **37**, 04023028 (2023).
25. *Weather Data & Weather API | Visual Crossing*. (n.d.). Retrieved September 20, 2023, from <https://www.visualcrossing.com>.
26. A'Terman, D. Z., & Dmitrukhin, A. F. Experience in the operation of hydraulic structures and equipment of hydroelectric stations. *Hydrotech. Constr.; (United States)*, **18**, (1984).
27. Raspini, F. et al. Continuous, semi-automatic monitoring of ground deformation using Sentinel-1 satellites. *Sci. Rep.* **8**, 7253 (2018).
28. Adamo, N., Al-Ansari, N., Sissakian, V., Laue, J. & Knutsson, S. Dam Safety: Sediments and Debris Problems. *J. Earth Sci. Geotech. Eng.* 27–63 (2020) <https://doi.org/10.47260/JESGE/1112>.
29. Zhang, L., Peng, M., Chang, D., & Xu, Y. *Dam failure mechanisms and risk assessment*. John Wiley & Sons. (2016).
30. *Committee on Dam Safety International Commission on Large Dams (ICOLD)*, “*ICOLD Incident Database Bulletin 99 Update - Statistical Analysis of Dam Failures*”, Accessed: Sep. 06, 2023. Available: <https://www.icoldchile.cl/boletines/188.pdf>.
31. Macchiarulo, V., Milillo, P., Blenkinsopp, C., Reale, C. & Giardina, G. Multi-temporal InSAR for transport infrastructure monitoring: recent trends and challenges. *Proc. Inst. Civil Eng.: Bridge Eng.* **176**, 92–117 (2021).
32. Hooper, A., Zebker, H., Segall, P. & Kampes, B. A new method for measuring deformation on volcanoes and other natural terrains using InSAR persistent scatterers. *Geophys. Res. Lett.* **31**, 1–5 (2004).
33. Perissin, D., Wang, Z. & Wang, T. The SARPROZ InSAR tool for urban subsidence/manmade structure stability monitoring in China. *Proceedings of the ISRSE*, Sydney, Australia, 1015 (2011).
34. *SARPROZ manual* (n.d.). Retrieved November 07, 2023, from <https://www.sarproz.com/software-manual/>.
35. Ferretti, A., Prati, C. & Rocca, F. Permanent scatterers in SAR interferometry. *IEEE Trans. Geosci. Remote Sens.* **39**, 8–20 (2001).
36. Estahbanati, A. T. & Dehghani, M. A phase unwrapping approach based on extended Kalman filter for subsidence monitoring using persistent scatterer time series interferometry. *IEEE J. Sel. Top. Appl. Earth Obs. Remote Sens.* **11**, 2814–2820 (2018).
37. Perissin, D., Wang, Z. & Lin, H. Shanghai subway tunnels and highways monitoring through Cosmo-SkyMed Persistent Scatterers. *ISPRS J. Photogr. Remote Sens.* **73**, 58–67 (2012).

Acknowledgements

We would like to extend my appreciation to the Copernicus programme for their invaluable contribution in making Sentinel-1 data freely accessible. This work was performed at the University of Houston under a contract with the Commercial Smallsat Data Scientific Analysis Program of NASA (NNH22ZDA001N-CSDSA) and the Decadal Survey Incubation Program: Science and Technology (NNH21ZDA001N-DSI). This publication is also part of the Vidi project InStruct, project number 18912, financed by the Dutch Research Council (NWO). We also want to thank anonymous reviewers for their helpful comments.

Author contributions

P.M. set up the Sentinel-1 experiment P.M. and A.T. analysed and processed the Sentinel-1 data. A.T. worked on the InSAR data post-processing P.M. and A.T. interpreted the results and wrote the manuscript. G.G. and H.K. worked on the structural engineering analysis. All authors reviewed the manuscript.

Competing interests

The authors declare no competing interests.

Additional information

Supplementary information The online version contains supplementary material available at <https://doi.org/10.1038/s43247-024-01284-z>.

Correspondence and requests for materials should be addressed to Amin Tavakkoliestahbanati.

Peer review information *Communications Earth & Environment* thanks Korniy Tretyak, Yusupujiang Aimaiti and the other, anonymous, reviewer(s) for their contribution to the peer review of this work. Primary Handling Editors: Heike Langenberg and Carolina Ortiz Guerrero. A peer review file is available.

Reprints and permissions information is available at <http://www.nature.com/reprints>

Publisher's note Springer Nature remains neutral with regard to jurisdictional claims in published maps and institutional affiliations.

Open Access This article is licensed under a Creative Commons Attribution 4.0 International License, which permits use, sharing, adaptation, distribution and reproduction in any medium or format, as long as you give appropriate credit to the original author(s) and the source, provide a link to the Creative Commons licence, and indicate if changes were made. The images or other third party material in this article are included in the article's Creative Commons licence, unless indicated otherwise in a credit line to the material. If material is not included in the article's Creative Commons licence and your intended use is not permitted by statutory regulation or exceeds the permitted use, you will need to obtain permission directly from the copyright holder. To view a copy of this licence, visit <http://creativecommons.org/licenses/by/4.0/>.

© The Author(s) 2024